EDGE ARTICLE

Check for updates

The role of L-histidine as molecular tongs: a strategy of grasping Tb³⁺ using ZIF-8 to design sensors for monitoring an anthrax biomarker on-the-spot†

Lan Guo, Maosheng Liang, Xiuli Wang, Rongmei Kong, Guang Chen, Lian Xia [iD] * and Fengli Qu [iD] *

In this study, a novel lanthanide-doped nanoprobe for monitoring dipicolinic acid (DPA), a unique biomarker of *Bacillus anthracis*, was constructed by coordination of Tb³⁺ with L-histidine (His) functionalized ZIF-8 (His@ZIF-8). After being functionalized with His, the resultant His@ZIF-8 had abundant carboxyl and amino groups, which like tongs help His@ZIF-8 "grasp" Tb³⁺ firmly to form a stable lanthanide-doped nanoparticle (His@ZIF-8/Tb³⁺). Owing to the unsaturated coordination of Tb³⁺ with the amino acid group, the resultant His@ZIF-8/Tb³⁺ showed reserved response sites of Tb³⁺ to DPA because of its unique molecular structure. After the His@ZIF-8/Tb³⁺ coordination with DPA, the intrinsic fluorescence emission of the Tb³⁺ ions was triggered through energy transfer, leading to bright yellow green luminescence owing to the antenna role of DPA. Benefitting from the His functionalization and the characteristics of ZIF-8, especially the high porosity and large surface area, the developed His@ZIF-8/Tb³⁺ sensing platform exhibited attractive features as a fluorescent sensor for monitoring DPA such as fast response kinetics (10 s), high sensitivity and selectivity, and being portable, easy to operate, economical and secure. This sensor platform showed a satisfactory linear relationship ($R^2 = 0.999$) ranging from 0.08 to 10 μmol L⁻¹ and an ultralow limit of detection (LOD) of 0.02 μmol L⁻¹. This strategy for the design of functionalized MOFs to construct sensing probes and the resultant His@ZIF-8/Tb³⁺ would provide a potential strategy for the exploitation of other functionalized materials used in other research fields and promising fluorescence platforms for the detection of other targets.

1. Introduction

Anthrax caused by *Bacillus anthracis* is an acute and infectious disease affecting humans and animals.[1] *Bacillus anthracis* mainly exists in the form of spores, which can survive in harsh conditions, such as high temperature, strong acids/bases and ultraviolet radiation.[2] It is reported that inhalation of more than 10^4 *Bacillus anthracis* spores can cause death unless effective therapeutic treatment is conducted within 24–48 h.[3,4] Thus, *Bacillus anthracis* spores not only lead to health problems and food poisoning,[5] but also serve as a potential bioterrorism reagent.[6] Fortunately, dipicolinic acid (DPA) has been determined to be a unique biomarker for anthrax.[7,8] Therefore, simple, fast, sensitive and selective methods for on-the-spot detection of DPA are particularly needed.

Lanthanide-doped nanoparticles show great potential for designing sensors owing to the preeminent optical properties of the lanthanide, such as long luminescence lifetime, large Stokes/anti-Stokes shift, sharp emission band, and so on.[9–14] In addition, the nanomaterial matrix also plays an important role in the complex, which acts as a host matrix to disperse the lanthanide and enhance light harvesting. In order to increase the doped amount and prevent the leakage of the lanthanide for the improvement of the sensitivity and stability of lanthanide-doped nanoparticles, matrix materials with characteristics of large specific surface area and high porosity, as well as plenty of uniform binding sites for the lanthanide with high affinity will be a perfect candidate.

Zeolitic imidazolate frameworks (ZIFs), a subclass of metal–organic frameworks (MOFs), are self-assembled from metal ions and imidazole linkers at room temperature.[15–21] The mild synthesis conditions, structural diversity, large specific surface area, high porosity, and high aqueous stability of ZIFs have made them very attractive for biochemical applications.[22–28] However, ZIFs lack high affinity binding sites for lanthanides, so the interaction between them is not strong enough to form a stable complex, which limits their application as a host matrix for composite lanthanide-doping nanoparticles. In order to take

advantage of MOF porosity and lanthanide spectral properties to construct a stable sensing platform, design of functionalized ZIFs with binding sites for lanthanides is one of the effective strategies. Fortunately, L-histidine (His), a common amino acid, possesses both an imidazole ring and amino acid group in one molecule. This unique structure endows His with high affinity towards Zn^{2+} to form ZIF nanostructures and ability to act as tongs for the amino acid group to grasp lanthanides through post coordination.

Herein, carboxyl and amine group bifunctionalized ZIF-8 (His@ZIF-8) was synthesized using His and 2-methylimidazole (Hmim) through a simple one-pot method to construct a sensing platform for monitoring DPA (Scheme 1). After being functionalized with His, His@ZIF-8 had abundant carboxyl and amine groups, which can firmly grasp Tb^{3+} ions to form a stable lanthanide-doped nanoparticle (His@ZIF-8/Tb^{3+}). Owing to the unsaturated coordination of Tb^{3+} with the amino acid group, the resultant His@ZIF-8/Tb^{3+} showed reserved response sites of Tb^{3+} to DPA because of its unique molecular structure. Therefore, when the His@ZIF-8/Tb^{3+} probe was dispersed in a buffer solution, the free coordination site of Tb^{3+} was occupied by H_2O molecules, and the probe showed no fluorescence emission, whereas, in the presence of DPA, the H_2O molecules combined with Tb^{3+} were substituted by DPA. Owing to the low triplet energy level of DPA $(3\pi\pi^*)$,[11,29–34] energy transfer from DPA to Tb^{3+} occurred easily. Therefore the intrinsic fluorescence of Tb^{3+} was sensitized, leading to bright yellow green fluorescence owing to the antenna role of DPA. The as-prepared His@ZIF-8/Tb^{3+}-based sensing platform possesses the following advantages: (1) the synthesis process was very simple and carried out at room temperature without using highly toxic reagents, such as Eriochrome Black T.[29] (2) The highly uniform nanoscale cavities and large surface area of His@ZIF-8 not only played an important role in specifically identifying targets but also promoted the target enrichment effect in their micropores, resulting in a lower detection limit and a higher sensing sensitivity. (3) The strategy used for functionalizing MOFs with natural amino acids to construct sensing probes is very fascinating, and will provide a beneficial reference for the modification of MOFs. (4) His@ZIF-8 has higher water solubility and stability than other MOFs, which will broaden its application in biological systems. (5) The sensing platform showed a satisfactory detection limit (0.02 μmol L^{-1}), excellent selectivity and
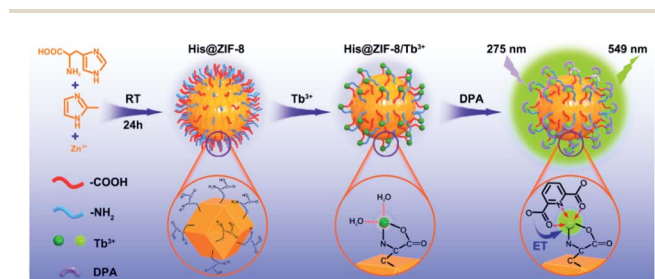
fast response kinetics (10 s), and it has been successfully applied to detect DPA in real samples, such as human urine and bovine serum. (6) The gel plate pre-treated with His@ZIF-8/Tb^{3+} can be used as test paper for monitoring DPA with the advantages of being portable, economical, secure and easy to operate, and having fast response kinetics. To the best of our knowledge, a ZIF-based fluorescence sensor for anthrax biomarker detection is developed for the first time. In addition, His functionalized ZIFs would provide a potential strategy for the exploitation of promising fluorescence platforms for the detection of other targets.
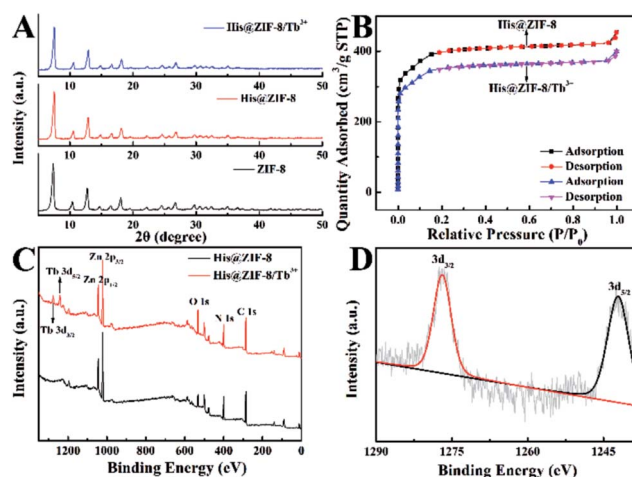
2. Results and discussion

2.1 Characterization of His@ZIF-8 and His@ZIF-8/Tb^{3+}

X-ray diffraction (XRD) patterns of His@ZIF-8 and His@ZIF-8/Tb^{3+} are shown in Fig. 1A. In Fig. 1A, the diffraction peaks of His@ZIF-8 and His@ZIF-8/Tb^{3+} were similar to that of ZIF-8, proving the successful preparation of His@ZIF-8 and His@ZIF-8/Tb^{3+} crystals. However, the typical characteristic peaks of His@ZIF-8 and His@ZIF-8/Tb^{3+} were slightly shifted to larger angles when compared to those of ZIF-8, demonstrating that both of them display the same sodalite topology as ZIF-8 with a slightly smaller unit cell. The peak shift was attributed to the incorporation of the amino acid, His, which caused slight lattice distortion in the crystal according to reported literature.[35–37] Moreover, the XRD peaks of His@ZIF-8/Tb^{3+} remained unchanged when compared with those of His@ZIF-8. This may be due to the coordination of Tb^{3+} with only the exposed carboxyl and amino groups of His@ZIF-8 without being incorporated into its framework.

The porosities of His@ZIF-8 and His@ZIF-8/Tb^{3+} were confirmed by using N_2 adsorption–desorption isotherms at 77 K (Fig. 1B). As shown in Fig. 1B, in the low pressure stage, the adsorption volume increased intensely with increasing

Fig. 1 (A) XRD spectra of the synthesized ZIF-8, His@ZIF-8 and His@ZIF-8/Tb^{3+}. (B) N_2 adsorption–desorption isotherms of the as-synthesized His@ZIF-8 and His@ZIF-8/Tb^{3+}. (C) The XPS spectra of His@ZIF-8 and His@ZIF-8/Tb^{3+}. (D) The high-resolution XPS spectrum of Tb 3d of His@ZIF-8/Tb^{3+}.

Scheme 1 Schematic diagram showing the fabrication process of His@ZIF-8/Tb^{3+} and its sensing mechanism of energy transfer (ET) with DPA.

pressure. However, after further increasing the pressure, the adsorption isotherms remained almost unchanged. This clearly showed that the adsorption–desorption process had typical type-I adsorption isotherm characteristics based on the IUPAC classification, indicating the microporous characters of the synthesized materials. In addition, the Brunauer–Emmett–Teller (BET) surface areas of His@ZIF-8 and His@ZIF-8/Tb^{3+} were 1304.34 m^2 g^{-1} and 1147.82 m^2 g^{-1}, respectively. The slightly lower nitrogen absorption volume of His@ZIF-8/Tb^{3+} than that of His@ZIF-8 was attributed to the coordination of Tb^{3+}. Such a high porosity and large BET surface area will contribute to the enhanced enrichment of targets in the test solution. To investigate the thermal stability of His@ZIF-8 and His@ZIF-8/Tb^{3+}, thermogravimetric analysis (TGA) was performed. As shown in Fig. S1,† both of them were stable even up to 400 °C, which was greatly beneficial for its practical application. Fourier transform infrared (FT-IR) spectroscopy (Fig. S2†) was carried out to identify the functional groups in His@ZIF-8 and His@ZIF-8/Tb^{3+}. Each spectrum in Fig. S2† shows an absorption peak at about 1600 cm^{-1}, which corresponded to the C=O stretching in the carboxyl group. Furthermore, an additional adsorption peak was found at about 1050 cm^{-1} for His@ZIF-8 and His@ZIF-8/Tb^{3+}, which corresponded to the amine group. However, the FT-IR spectrum of ZIF-8 did not show this adsorption peak. The above results demonstrated that His@ZIF-8 and His@ZIF-8/Tb^{3+} were successfully functionalized with amino and carboxyl groups. Fig. 1C shows X-ray photoelectron spectroscopy (XPS) characterization of His@ZIF-8 before and after being coordinated with Tb^{3+}. As shown in Fig. 1C, two new photoelectron peaks at 1242.1 eV and 1276.8 eV were observed for His@ZIF-8/Tb^{3+}, which were due to Tb 3d$_{3/2}$ and Tb 3d$_{5/2}$, confirming the successful preparation of His@ZIF-8/Tb^{3+}. The high-resolution XPS spectrum of Tb 3d (Fig. 1D) further verified the above conclusion. The coordination of Tb^{3+} with His@ZIF-8 was also confirmed using zeta potential (Fig. S3†). The zeta potential of His@ZIF-8/Tb^{3+} (5.86 mV) exhibited a significant increase in comparison with that of His@ZIF-8 (−8.51 mV), which demonstrated that Tb^{3+} was captured by His@ZIF-8.

The structural morphologies of His@ZIF-8 before and after being coordinated with Tb^{3+} were characterized by scanning electron microscopy (SEM). As shown in Fig. S4,† the His@ZIF-8 crystal was a regular diamond dodecahedron with an average diameter of about 600 nm (Fig. S4A†). After coordination with Tb^{3+}, the crystal structure of His@ZIF-8 still remained well (Fig. S4B†). This indicated that the coordination of Tb^{3+} had no influence on the structure of His@ZIF-8. Moreover, the well-defined diamond dodecahedron structure was also obtained by transmission electron microscopy (TEM) characterization (Fig. 2A and B). The scanning TEM (STEM) elemental mapping shown in Fig. 2C indicated that the characteristic elements, including C, N, O and Zn, were all present and homogeneously distributed in His@ZIF-8. The existence of Tb^{3+} in His@ZIF-8/Tb^{3+} was further confirmed by elemental mapping. As shown in Fig. 2D, Tb^{3+} was evenly distributed in the material, which was consistent with the energy dispersive X-ray (EDX) analysis (Fig. S5†).
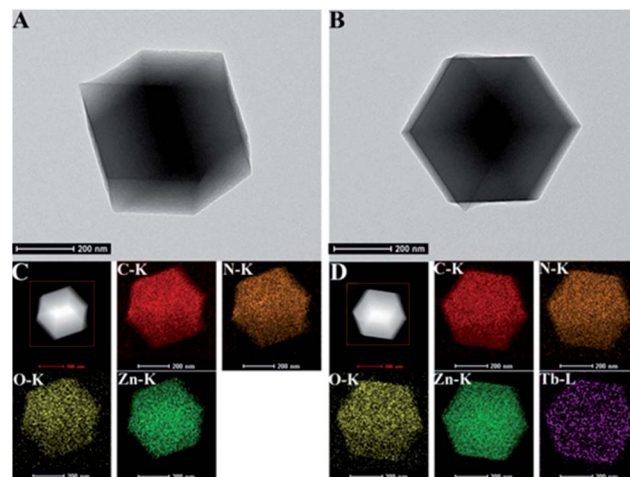

Fig. 2 TEM images of His@ZIF-8 (A) and His@ZIF-8/Tb^{3+} (B). Dark field STEM and elemental mapping images of His@ZIF-8 (C) and His@ZIF-8/Tb^{3+} (D).

2.2 Optimization of the experimental conditions

In order to obtain the optimum conditions for sensing DPA, the experimental parameters including pH values and incubation time were systematically optimized. First, fluorescence experiments were carried out in HEPES buffer solutions with different pH values (4, 5, 6, 7, 7.4, 8, 9 and 10) (Fig. S6A†). As shown in Fig. S6A,† the fluorescence intensity of both His@ZIF-8/Tb^{3+} and His@ZIF-8/Tb^{3+} + DPA solutions increased slightly in the case of pH values higher than 7.0. Furthermore, the fluorescence intensity remained steady in the pH range of 7.4–9.0. Since 7.4 is physiological pH, we chose pH 7.4 as the optimal pH value for the detection of DPA. Next, the kinetics of the probe response to the target DPA was studied using His@ZIF-8/Tb^{3+}. The result in Fig. S6B† showed that the response of His@ZIF-8/Tb^{3+} to DPA reached equilibrium immediately within 10 s. The fast response of His@ZIF-8/Tb^{3+} to DPA may originate from the large surface area and the abundant pores of ZIF-8, which facilitated the interaction of His@ZIF-8/Tb^{3+} with DPA owing to the adsorption effect. In general, the optimal parameters were determined to be a pH value of 7.4 and a response time of 10 s.

2.3 Optical response of His@ZIF-8/Tb^{3+} as a nanoprobe for DPA detection

The feasibility of using His@ZIF-8 for fluorescence detection of DPA was systematically studied. The coordination of DPA with His@ZIF-8/Tb^{3+} was first verified using zeta potential changes. As shown in Fig. S3,† the zeta value of His@ZIF-8/Tb^{3+} showed an obvious decline from 5.86 to 3.39 mV upon addition of 1 μmol L^{-1} DPA, indicating that DPA was successfully coordinated with His@ZIF-8/Tb^{3+}. The sensitizer effect of DPA on His@ZIF-8/Tb^{3+} was then investigated using UV-vis spectroscopy. As shown in Fig. 3A, His@ZIF-8/Tb^{3+} solution had no UV absorption peak. Interestingly, after being coordinated with DPA, the His@ZIF-8/Tb^{3+} aqueous solution presented the intrinsic absorption of DPA. Then the fluorescence emission
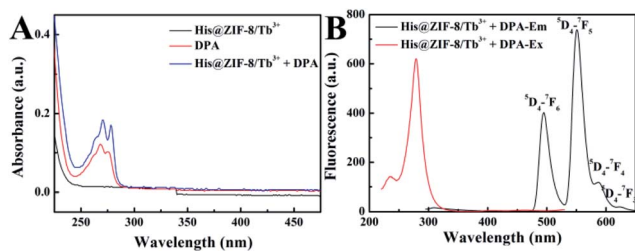
Fig. 3 (A) UV-vis absorption spectra of His@ZIF-8/Tb^{3+} (0.05 g L^{-1}), DPA (1 μmol L^{-1}) and His@ZIF-8/Tb^{3+} (0.05 g L^{-1}) in the presence of 1 μmol L^{-1} DPA. (B) Excitation and emission spectra of His@ZIF-8/Tb^{3+} in the presence of DPA (1 μmol L^{-1}).

spectrum of His@ZIF-8/Tb^{3+} after coordination with DPA was investigated. Under the excitation of 275 nm, His@ZIF-8/Tb^{3+}/DPA exhibited emission bands at 495 nm ($^5D_4-^7F_6$), 549 nm ($^5D_4-^7F_5$), 587 nm ($^5D_4-^7F_4$), and 623 nm ($^5D_4-^7F_3$), respectively (Fig. 3B). These results confirmed that the Tb^{3+} ions were sensitized by the "antenna" molecules of DPA. Moreover, in order to validate the important role of His, the response abilities of ZIF-8/Tb^{3+} and His@ZIF-8/Tb^{3+} to DPA were compared. As shown in Fig. S7A,† after interaction with DPA (1 μmol L^{-1}), the fluorescence of ZIF-8/Tb^{3+} increased slightly, indicating that there were trace amounts of Tb^{3+} combined with ZIF-8. The probable reason is that Tb^{3+} can be adsorbed on the surface of ZIF-8 owing to its characteristics of porosity and a large surface area. However, the fluorescence of His@ZIF-8/Tb^{3+}enhanced significantly after adding 1 μmol L^{-1} DPA (Fig. S7B†). As shown in Fig. S7C,† the sensitivity [$(F - F_0)/F_0$] of His@ZIF-8/Tb^{3+} towards DPA was 4.6 times higher than that of ZIF-8/Tb^{3+}. This indicated that His@ZIF-8 has much higher capability of capturing Tb^{3+} than ZIF-8, benefitting from the amino and carboxyl groups by doping His into ZIF-8.

Under the optimal conditions, the sensing performance of His@ZIF-8/Tb^{3+} towards DPA was examined. The fluorescence intensities of His@ZIF-8/Tb^{3+} treated with various concentrations of DPA (0, 0.08, 0.1, 0.2, 0.4, 0.6, 0.8, 1, 2, 4, 6, 8 and 10 μmol L^{-1}) in HEPES buffer (20 mmol L^{-1}, pH 7.4) were assessed. As shown in Fig. 4A and B, the fluorescence intensity at 544 nm increased gradually with the addition of DPA. Especially, a good linear relationship between the fluorescence intensity and the DPA concentration ($F = 529.29C + 235.89$; $R^2 = 0.999$) was successfully achieved in the DPA concentration range of 0.08–10 μmol L^{-1}. Moreover, the limit of detection (LOD) for DPA, at a signal-to-noise (S/N) ratio of 3, was calculated to be 0.02 μmol L^{-1}, which was lower than 1–3000th of the infectious dose of the spores (60 μmol L^{-1}). For evaluating the emitting color change of His@ZIF-8/Tb^{3+} with respect to the DPA content, the Commission Internationale de L'Eclairage (CIE) coordinates of the emission spectra of His@ZIF-8/Tb^{3+} suspensions with different DPA concentrations were calculated (Fig. 4C). It clearly shows that the calculated chromaticity moved from yellow to green. In addition, to highlight the application of the proposed sensor in our study for the determination of DPA, the performance of our sensing platform was compared with that of previously reported sensors for the detection of DPA (Table S1†).
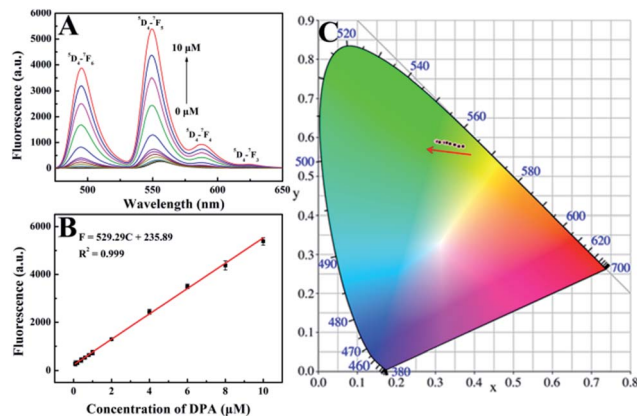

Fig. 4 (A) Fluorescence emission spectra of His@ZIF-8/Tb^{3+} for various concentrations of DPA (0, 0.08, 0.1, 0.2, 0.4, 0.6, 0.8, 1, 2, 4, 6, 8 and 10 μmol L^{-1}). (B) Linear relationship of fluorescence intensity at 544 nm with DPA concentration. (C) CIE chromaticity coordinates calculated from the emission spectra that are presented in A with increasing DPA concentration from 0 to 10 μmol L^{-1}.

The results showed that this proposed sensor exhibited advantages of a simple preparation process, low LOD, broad linear range, and fast response capability.

Selectivity is another indispensable factor for the practical application of a sensing platform. So we investigated the fluorescence responses of His@ZIF-8/Tb^{3+} to potential interfering substances, including Na$^+$, K$^+$, Ca^{2+}, Mg^{2+}, Cl$^-$, CO$_3^{2-}$, SO$_4^{2-}$, Phe, Cys, Glu, BA, o-PA and p-PA (10^{-4} mol L^{-1}). As shown in Fig. 5, it was clear that there were negligible fluorescence changes after mixing with the possible interferents, some of which even have a similar structure to DPA. Such results indicated that the proposed probe His@ZIF-8/Tb^{3+} had highly specific recognition towards DPA, revealing the high selectivity of the method. The outstanding selectivity was derived from the unique structural characteristics of DPA, which offered binding
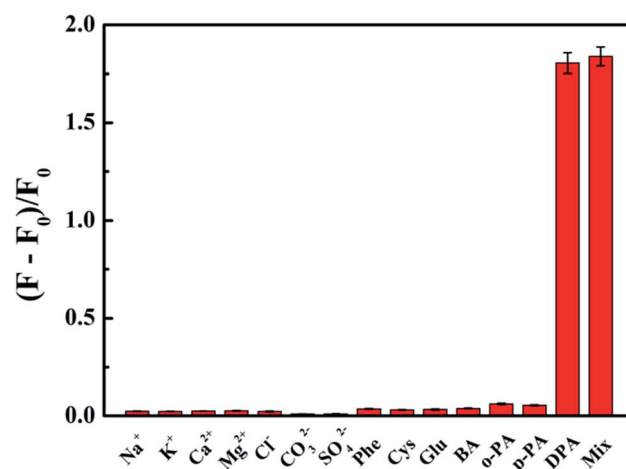

Fig. 5 Two-dimensional optical density graph of His@ZIF-8/Tb^{3+} at 544 nm upon addition of 1×10^{-6} mol L^{-1} DPA, 1×10^{-4} mol L^{-1} other potential interferents (Na$^+$, K$^+$, Ca^{2+}, Mg^{2+}, Cl$^-$, CO$_3^{2-}$, SO$_4^{2-}$, Phe, Cys, Glu, BA, o-PA and p-PA) and a mixture of them.

sites of O (carboxylate) and N (aromatic ring) to coordinate tightly with Tb^{3+}. Therefore, H_2O molecules combined with Tb^{3+} via weak coordination can be replaced easily. The above results demonstrate the promising application of the designed His@-ZIF-8/Tb^{3+} for sensing DPA in actual specimens.

2.4 The stability of His@ZIF-8/Tb^{3+}

In addition to excellent DPA detection performance, His@ZIF-8/Tb^{3+} also showed good stability for sensing DPA. Fig. S8A and B† show that the His@ZIF-8/Tb^{3+} crystals stayed intact after the detection of DPA, which might be attributed to the stable characteristics of ZIF-8 and the rapid response kinetics of the sensing platform. The XRD patterns further verified that the crystal structure of His@ZIF-8/Tb^{3+} remained unchanged after the detection of DPA (Fig. S8C†).

2.5 Application of His@ZIF-8/Tb^{3+} in real samples

To investigate the detection practicability of His@ZIF-8/Tb^{3+}, assays were carried out to detect DPA in both human urine and 10% bovine serum. As shown in Table S2,† no DPA was directly detected in the above real samples. Subsequently, both of the above samples were spiked with DPA at three levels: 0.50, 1.00 and 5.00 μmol L^{-1} and then detection was performed. The results showed that the recoveries of DPA ranged from 98.0 to 103.2% with RSDs less than 5%, suggesting the high analytical accuracy and precision of the established method.

In order to further study the practical application of the proposed sensor, silica gel plates were immersed in His@ZIF-8/Tb^{3+} dispersions (0.1 g L^{-1}) as test paper for detecting DPA. We wrote "QFNU" on the silica gel sheets using the solutions of Na^+, K^+, Ca^{2+}, Mg^{2+}, Cl^-, CO_3^{2-}, SO_4^{2-}, Phe, Cys, Glu, BA, o-PA, and p-PA (100 μmol L^{-1}) and DPA (10 μmol L^{-1}) as ink, respectively (Fig. 6). As shown in Fig. 6A, all the plates showed no color change under visible light. Fascinatingly, as shown in Fig. 6B, under a UV lamp with a 254 nm wavelength, the plate written with DPA exhibited bright yellow green fluorescence with the script "QFNU", whereas the gel plates written with other potential interferent solutions showed no color change. These results indicate that the gel plate pretreated with His@ZIF-8/
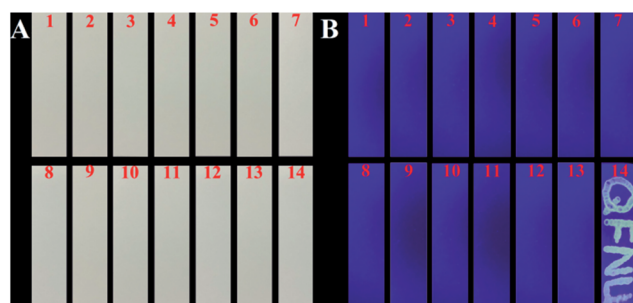

Fig. 6 Colors of silica gel plates under illumination of visible light (A) and a 254 nm UV lamp (B) upon writing using various analyte solutions [1, Na^+; 2, K^+; 3, Ca^{2+}; 4, Mg^{2+}; 5, Cl^-; 6, CO_3^{2-}; 7, SO_4^{2-}; 8, Phe; 9, Cys; 10, Glu; 11, BA; 12, o-PA; 13, p-PA; 14, DPA (100 μmol L^{-1}, except the concentration of DPA which was 10 μmol L^{-1})].

Tb^{3+} can be used as test paper for monitoring DPA with the advantages of being portable, easy to operate, economical, secure, and efficient.

3. Conclusions

In conclusion, we successfully proposed His functionalized ZIF-8 (His@ZIF-8) to improve its capacity of capturing Tb^{3+} and to construct a sensing probe for detecting an anthrax biomarker, DPA. After being functionalized with His, the resultant His@-ZIF-8 had abundant carboxyl and amine groups, which will help His@ZIF-8 capture Tb^{3+} much more effectively than bare ZIF-8. The functionalization with His and the high porosity and surface area of ZIF-8 led to much higher sensitivity and fast response kinetics of the detection method. This developed probe His@ZIF-8/Tb^{3+} for detecting DPA exhibited a few advantages, such as a one-pot synthesis procedure, high sensitivity and selectivity, fast response kinetics, and being portable, easy to operate, economical and secure. Especially, the practical applications of this probe for sensing DPA in human urine and bovine serum gave satisfactory results. We believe that His functionalized ZIFs would provide a potential strategy for the exploitation of promising fluorescence platforms for the detection of other targets.

4. Experimental section

4.1 Instruments and reagents

X-ray diffraction (XRD) patterns were obtained on a MiniFlex600 X-ray diffractometer. Scanning electron microscopy (SEM) images were collected by using a Sigma 500/vp scanning electron microscope. Transmission electron microscopy (TEM) measurements were performed with a transmission electron microscope (JEOL 2010) and scanning TEM (STEM) elemental mapping was performed using the same electron microscope equipped with an energy dispersive X-ray (EDX) spectrometer. Fourier transform infrared (FT-IR) spectroscopy was carried out on a Nicolet iS5 Fourier transform infrared spectrometer. N_2 adsorption–desorption curves were obtained using a Kubo-x1000 specific surface area and an aperture analyzer. X-ray photoelectron spectroscopy (XPS) analyses were carried out by using an ESCALAB 250Xi spectrometer. Thermogravimetric analysis (TGA) was carried out by using a Netzsch STA 449 F3 Jupiter. Fluorescence spectra were recorded on a Hitachi F-7000 fluorescence spectrophotometer in the wavelength range of 295–650 nm (emission slit width: 5 nm; excitation slit width: 10 nm; photomultiplier voltage: 400 V). $Zn(NO_3)_2 \cdot 6H_2O$, L-histidine (His), 2-methylimidazole (Hmim), trimethylamine (TEA) and methanol (MeOH) were bought from Sigma-Aldrich. And all the other chemical reagents were of analytical reagent grade and used without any treatment.

4.2 Synthesis of His@ZIF-8 crystals and His@ZIF-8/Tb^{3+}

His@ZIF-8 was prepared according to a recent report.[37] Briefly, 3.0 mmol His was dissolved in 40 mL deionized water. 250 μL of TEA was then added into the His solution and stirred for 5 min.

6.0 mmol Zn(NO$_3$)$_2$·6H$_2$O and 21.0 mmol Hmim were dissolved in 100 mL and 60 mL methanol, respectively. To prepare the MOF precursor solution, Hmim solution was first mixed and stirred with His solution for 15 min, followed by the addition of Zn(NO$_3$)$_2$·6H$_2$O solution. The solution was stirred for 24 h at room temperature. The product was collected by centrifugation at 7000 rpm for 5 min and repeatedly washed with methanol 3 times. The collected white powder was dried in an oven at 60 °C overnight.

The synthesis of His@ZIF-8/Tb^{3+} was performed by dispersing 30.0 mg His@ZIF-8 in 60.0 mL Tb(NO$_3$)$_3$ ethanol solution (10 mmol L^{-1}). Then the above solution was stirred for 2 h at room temperature. The product was collected by centrifugation at 7000 rpm for 5 min and repeatedly washed with ethanol 3 times. The collected white powder was dried in an oven at 60 °C overnight.

4.3 Fluorescence detection of DPA

In a typical run, 100 μL His@ZIF-8/Tb^{3+} (0.05 g L^{-1}), 800 μL HEPES buffer (20 mmol L^{-1}, pH 7.4) and 100 μL DPA with various concentrations (0–10 μmol L^{-1}) were mixed well and shook for 10 s. Then the solutions were transferred to a quartz cuvette for fluorescence measurements with excitation at 275 nm at room temperature.

4.4 Selectivity tests

In order to determine the selectivity of His@ZIF-8/Tb^{3+} for sensing DPA, the fluorescence emission spectra of 100 μL His@ZIF-8/Tb^{3+} (0.05 g L^{-1}), 800 μL HEPES buffer (20 mmol L^{-1}, pH 7.4) and 100 μL different potential interferents (1 × 10^{-4} mol L^{-1}) including Na$^+$, K$^+$, Ca^{2+}, Mg^{2+}, Cl$^-$, CO$_3^{2-}$, SO$_4^{2-}$, phenylalanine (Phe), cysteine (Cys), glucose (Glu), benzoic acid (BA), isophthalic acid (o-PA) and terephthalic acid (p-PA) were recorded.

4.5 Detection of DPA in real samples

For DPA detection in real samples, human urine was obtained from Qufu People's Hospital and the bovine serum sample was obtained commercially. All experiments were performed in compliance with the Ethical Laws of the People's Republic of China. The experimental procedure for the present study has been approved by the ethical committee of Qufu Normal University, China, and informed consent from volunteers was obtained for any experimentation with human subjects. The urine sample was filtered with a 0.45 μm microfiltration membrane for removing any potential particulate suspension. The bovine serum sample was used after deproteinization. During the analysis, 100 μL human urine or 100 μL 10% bovine serum [diluted with HEPES buffer (20 mmol L^{-1}, pH 7.4)], 100 μL different concentrations of DPA solution (0, 0.50, 1.00, and 5.00 μmol L^{-1}), 100 μL His@ZIF-8/Tb^{3+} (0.05 g L^{-1}) and 700 μL of HEPES buffer solution (20 mmol L^{-1}, pH 7.4) were added in sequence to form 1 mL of test solution, and the other procedures were the same as the above DPA assay. In the test solution, human urine was finally diluted 10 times, and bovine serum was finally diluted 100 times. All the experiments were carried out in triplicate.

Conflicts of interest

There are no conflicts to declare.

Acknowledgements

Notes and references

1 A. K. Goel, *World J. Clin. Cases*, 2015, **3**, 20–33.
2 H. Albert, D. J. G. Davies, L. P. Woodson and C. J. Soper, *J. Appl. Microbiol.*, 1998, **85**, 865–874.
3 B. H. Zhang, H. S. Wang, L. H. Lu, K. L. Ai, G. Zhang and X. L. Cheng, *Adv. Funct. Mater.*, 2008, **18**, 2348–2355.
4 W. Hurtle, E. Bode, D. A. Kulesh, R. S. Kaplan, J. Garrison, D. Bridge, M. House, M. S. Frye, B. Loveless and D. Norwood, *J. Clin. Microbiol.*, 2004, **42**, 179–185.
5 P. T. Yung, E. D. Lester, G. Bearman and A. Ponce, *Biotechnol. Bioeng.*, 2007, **98**, 864–871.
6 M. Enserink, *Science*, 2001, **294**, 490–491.
7 R. Goodacre, B. Shann, R. J. Gilbert, E. M. Timmins, A. C. McGovern, B. K. Alsberg, D. B. Kell and N. A. Logan, *Anal. Chem.*, 2000, **72**, 119–127.
8 K. L. Ai, B. H. Zhang and L. H. Lu, *Angew. Chem., Int. Ed.*, 2009, **48**, 304–308.
9 Y. S. Liu, S. Y. Zhou, D. T. Tu, Z. Chen, M. D. Huang, H. M. Zhu, E. Ma and X. Y. Chen, *J. Am. Chem. Soc.*, 2012, **134**, 15083–15090.
10 H. Ma, B. Song, Y. X. Wang, D. Y. Cong, Y. F. Jiang and J. L. Yuan, *Chem. Sci.*, 2017, **8**, 150–159.
11 K. Luan, R. Q. Meng, C. F. Shan, J. Cao, J. G. Jia, W. S. Liu and Y. Tang, *Anal. Chem.*, 2018, **90**, 3600–3607.
12 J. Xu, S. Y. Zhou, D. T. Tu, W. Zheng, P. Huang, R. F. Li, Z. Chen, M. D. Huang and X. Y. Chen, *Chem. Sci.*, 2016, **7**, 2572–2578.
13 Q. Ju, D. T. Tu, Y. S. Liu, R. F. Li, H. M. Zhu, J. C. Chen, Z. Chen, M. D. Huang and X. Y. Chen, *J. Am. Chem. Soc.*, 2012, **134**, 1323–1330.
14 P. C. Huang, F. Y. Wu and L. Q. Mao, *Anal. Chem.*, 2015, **87**, 6834–6841.
15 D. Saliba, M. Ammar, M. Rammal, M. Al-Ghoul and M. Hmadeh, *J. Am. Chem. Soc.*, 2018, **140**, 1812–1823.
16 S. S. Sankar, K. Karthick, K. Sangeetha and S. Kundu, *Inorg. Chem.*, 2019, **58**, 13826–13835.

17 K. Huang, Q. Q. Li, G. P. Liu, J. Shen, K. C. Guan and W. Q. Jin, *ACS Appl. Mater. Interfaces*, 2015, **7**, 16157–16160.

18 H. J. Hou and H. Q. Li, *J. Phys. Chem. C*, 2010, **114**, 13501–13508.

19 S. Tanaka and Y. Tanaka, *ACS Omega*, 2019, **4**, 19905–19912.

20 W. X. Cai, T. Lee, M. Lee, W. Cho, D. Y. Han, N. Choi, A. C. K. Yip and J. Choi, *J. Am. Chem. Soc.*, 2014, **136**, 7961–7971.

21 G. Khandelwal, A. Chandrasekhar, N. P. M. J. Raj and S. Kim, *Adv. Energy Mater.*, 2019, **9**, 1803581.

22 J. E. Ellis, Z. Zeng, S. I. Hwang, S. B. Li, T. Y. Luo, S. C. Burkert, D. L. White, N. L. Rosi, J. J. Gassensmith and A. Star, *Chem. Sci.*, 2019, **10**, 737–742.

23 J. Lopez-Cabrelles, J. Romero, G. Abellán, M. Giménez-Marqués, M. Palomino, S. Valencia, F. Rey and G. M. Espallargas, *J. Am. Chem. Soc.*, 2019, **141**, 7173–7180.

24 J. J. Deng, K. Wang, M. Wang, P. Yu and L. Q. Mao, *J. Am. Chem. Soc.*, 2017, **139**, 5877–5882.

25 X. R. Chen, D. Liu, G. J. Cao, Y. Tang and C. Wu, *ACS Appl. Mater. Interfaces*, 2019, **11**, 9374–9384.

26 N. K. Maddigan, A. Tarzia, D. M. Huang, C. J. Sumby, S. G. Bell, P. Falcaro and C. J. Doonan, *Chem. Sci.*, 2018, **9**, 4217–4223.

27 Z. H. Zhao, T. R. Lin, W. R. Liu, L. Hou, F. G. Ye and S. L. Zhao, *Spectrochim. Acta, Part A*, 2019, **219**, 240–247.

28 H. G. Jin, W. B. Zong, L. Yuan and X. B. Zhang, *New J. Chem.*, 2018, **42**, 12549–12556.

29 M. D. Yilmaz and H. A. Oktem, *Anal. Chem.*, 2018, **90**, 4221–4225.

30 Y. Q. Luo, L. Zhang, L. Y. Zhang, B. H. Yu, Y. J. Wang and W. B. Zhang, *ACS Appl. Mater. Interfaces*, 2019, **11**, 15998–16005.

31 Q. Li, K. Sun, K. W. Chang, J. B. Yu, D. T. Chiu, C. F. Wu and W. P. Qin, *Anal. Chem.*, 2013, **85**, 9087–9091.

32 H. Chen, Y. J. Xie, A. M. Kirillov, L. L. Liu, M. H. Yu, W. S. Liu and Y. Tang, *Chem. Commun.*, 2015, **51**, 5036–5039.

33 Q. X. Wang, S. F. Xue, Z. H. Chen, S. H. Ma, S. Q. Zhang, G. Y. Shi and M. Zhang, *Biosens. Bioelectron.*, 2017, **94**, 388–393.

34 Y. H. Zhang, B. Li, H. P. Ma, L. M. Zhang and Y. X. Zhen, *Biosens. Bioelectron.*, 2016, **85**, 287–293.

35 S. Borukhin, L. Bloch, T. Radlauer, A. H. Hill, A. N. Fitch and B. Pokroy, *Adv. Funct. Mater.*, 2012, **22**, 4216–4224.

36 R. A. Brif, L. Bloch and B. Pokroy, *CrystEngComm*, 2014, **16**, 3268–3273.

37 J. Y. Chan, H. Zhang, Y. Nolvachai, Y. X. Hu, H. J. Zhu, M. Forsyth, Q. F. Gu, D. E. Hoke, X. W. Zhang, P. J. Marriot and H. T. Wang, *Angew. Chem., Int. Ed.*, 2018, **130**, 17376–17380.